

We are IntechOpen, the world's leading publisher of Open Access books Built by scientists, for scientists

4,800

Open access books available

122,000

International authors and editors

135M

Downloads

Our authors are among the

154

Countries delivered to

TOP 1%

most cited scientists

12.2%

Contributors from top 500 universities



WEB OF SCIENCE™

Selection of our books indexed in the Book Citation Index
in Web of Science™ Core Collection (BKCI)

Interested in publishing with us?
Contact book.department@intechopen.com

Numbers displayed above are based on latest data collected.
For more information visit www.intechopen.com



Engineering 3D Multi-Branched Nanostructures for Ultra-Sensing Applications

Anisha Chirumamilla, Manohar Chirumamilla,
Alexander S. Roberts, Andrea Cerea, Esben Skovsen,
Francesco De Angelis, Remo Proietti Zaccaria,
Peter Kjær Kristensen, Roman Krahne,
Duncan S. Sutherland, Sergey I. Bozhevolnyi,
Kjeld Pedersen and Andrea Toma

Additional information is available at the end of the chapter

<http://dx.doi.org/10.5772/intechopen.74066>

Abstract

The fabrication of plasmonic nanostructures with sub-10 nm gaps supporting extremely large electric field enhancement (hot-spot) has attained great interest over the past years, especially in ultra-sensing applications. The “hot-spot” concept has been successfully implemented in surface-enhanced Raman spectroscopy (SERS) through the extensive exploitation of localized surface plasmon resonances. However, the detection of analyte molecules at ultra-low concentrations, i.e., down to the single/few molecule level, still remains an open challenge due to the poor localization of analyte molecules onto the hot-spot region. On the other hand, three-dimensional nanostructures with multiple branches have been recently introduced, demonstrating breakthrough performances in hot-spot-mediated ultra-sensitive detection. Multi-branched nanostructures support high hot-spot densities with large electromagnetic (EM) fields at the interparticle separations and sharp edges, and exhibit excellent uniformity and morphological homogeneity, thus allowing for unprecedented reproducibility in the SERS signals. 3D multi-branched nanostructures with various configurations are engineered for high hot-spot density SERS substrates, showing an enhancement factor of 10^{11} with a low detection limit of 1 fM. In this view, multi-branched nanostructures assume enormous importance in analyte detection at ultra-low concentrations, where the superior hot-spot density can promote the identification of probe molecules with increased contrast and spatial resolution.

Keywords: hot-spot engineering, 3D multi-branched nanostructures, nanostars, top-down fabrication methods, ultra-sensitive SERS substrates

1. Introduction

Nanoplasmonics is an emerging area of scientific research with a variety of applications in spectroscopy, metamaterials engineering, biosensing, lasing, photocatalysis, nonlinear and quantum optics [1–8]. This discipline deals with the study of collective oscillations of conduction electrons at metal-dielectric interfaces, which can be resonantly excited upon external irradiation. Coupling of electromagnetic (EM) fields to the free-electron motion leads to enhanced optical near fields, confined in subwavelength regions and localized in close proximity of metallic nanoparticles (localized surface plasmon resonances—LSPRs), which are very sensitive to the local dielectric environment [9, 10]. Within this context, nanostructures endowed with sharp tips/edges and sub-10 nm interparticle separation (IPS) are ideal candidates for nanoscale manipulation of optical energy, promoting nanofocusing of EM radiation into hot-spots [11–15]. In recent years, a great variety of nanostructure geometries, for instance, nanospheres, nanocubes, nanocones, nanoantennas, nanoaggregates and nanostars, have been fabricated by bottom-up and top-down approaches [16–24], in order to engineer their plasmonic resonances and increase the field enhancement and hot-spot densities. Control over nanostructure morphology shows promising applications in bio/chemical sensing using the synergistic combination of LSPR and surface-enhanced Raman spectroscopy (SERS) as detection paradigm [9, 25–26].

As shown in **Figure 1**, the interaction of the incident light with a plasmonic nanostructure can promote resonant oscillation of the free electron cloud, which, for particles smaller than the exciting wavelength, can give rise to standing waves, i.e., to LSPRs. Noble metals, such as gold, silver and copper, are the best candidates for supporting plasmon activity, due to their low electron losses, high carrier densities and high field amplitudes on the particle surface. The nanostructure morphology (size, shape and arrangement) together with the surrounding dielectric environment plays a key role in the excitation of plasmonic resonances [10]. In LSPR-based sensing devices, the analytes adsorbed on the nanostructure

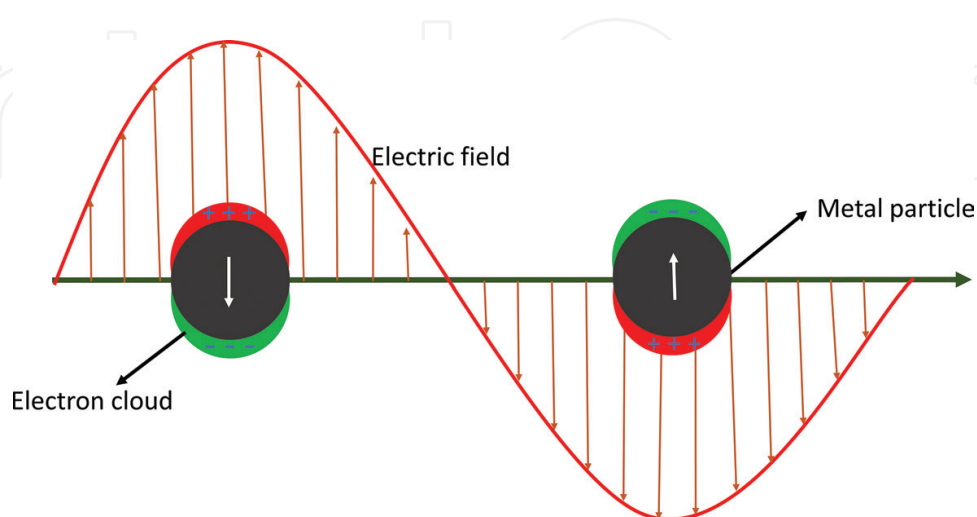


Figure 1. Schematic representation of the localized surface plasmon resonance on a metal particle.

surface influence the surrounding dielectric medium, thus resulting in an effective refractive index change and subsequent resonance shift. Although this technique is very powerful for molecule detection, it lacks analyte specificity, and it suffers from reduced efficiency at very small concentrations.

On the contrary, SERS enables the detection of biological and chemical analytes with high specificity and sensitivity even at ultra-low concentrations, exploiting the electromagnetic enhancement offered by plasmonic nanostructures [3, 27–32]. The huge enhancement typical of SERS substrates is mainly based on chemical and electromagnetic phenomena. In chemical enhancement [33], the charge transfer between electronic energy levels of the metal and the adsorbed molecules increases the Raman scattering cross-section up to a factor of 10^2 . The electromagnetic contribution, instead, is crucially depending on the near-field intensity associated with the nanostructure plasmonic activity. In SERS detection, the intrinsically weak Raman signals can be enhanced by many orders of magnitude (a factor of 10^8 has been observed in [34, 35]), due to the interaction between the adsorbed molecules and the electromagnetic near-fields. In this respect, nanostructures featuring closely spaced gaps and/or sharp protrusions are of great interest in detecting analytes at ultra-low concentration [8, 36, 37]. However, the tiny availability of molecules at the single/few entities limit can dramatically reduce the effectiveness of a plasmon-based sensitive device. It is therefore imperative for overcoming this practical limitation to design and engineer nanostructure architectures with sufficiently high hot-spot densities. **Figure 2** shows the local EM field mapping on a multi-branched (MB) nanoparticle using electron energy loss spectroscopy: strong near-field intensities are clearly promoted and well-confined by the sharp apices. In view of that, nanostructures with different layouts, multiple branches and single-digit IPS will be studied in the present work.

Various nanofabrication methods, applying both bottom-up and top-down approaches, have been used to fabricate SERS-based platforms for sensing applications [38–46]. Among them, colloidal techniques provide a wide variety of nanoparticles with sharp protrusions, although they are still suffering for poor control over uniformity and arrangement [35]. The positioning of the analyte molecule in the vicinity of the hot-spot is critical for improving the SERS enhancement factor and hence the detection limit. Due to the lack of reproducible

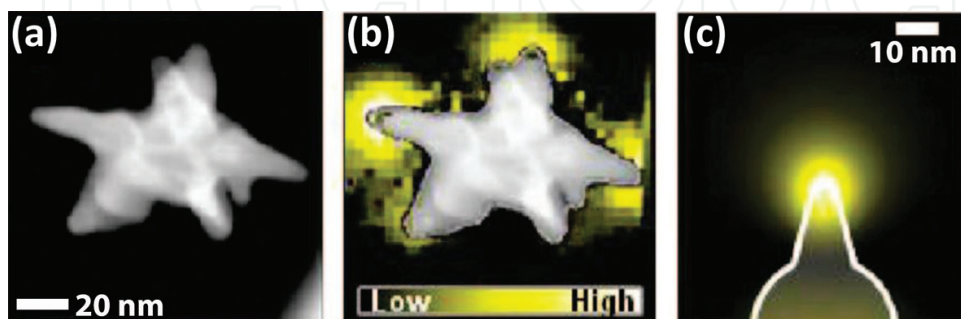


Figure 2. (a) Scanning transmission electron microscopy dark-field image of an individual gold nanostar. (b and c) Electron energy loss spectroscopy intensity mapping and the calculated intensity map of the plasmon resonances around a nanostar apex, respectively. Reprinted with permission from [35]. Copyright (2009) American Chemical Society.

SERS signals and homogeneity of the structures, alternative fabrication methods are needed. In this context, lithographic techniques can overcome these limitations, thus providing a feasible strategy towards the realization of uniformly patterned nanostructures over large areas. In the present chapter, fabrication and characterization of three-dimensional (3D) multi-branched plasmonic architectures realized by means of electron-beam lithography (EBL) and reactive ion etching (RIE) techniques will be investigated. Numerical calculations, Raman and optical characterization will be used for demonstrating outstanding performances in analyte detection at ultra-low concentrations.

2. Experimental techniques

2.1. Fabrication of multi-branched nanostructures

Figure 3a–c shows the fabrication protocol of typical six-branched nanostructures with 2D and 3D layout (without and with perforated metal (PM) topologies). A combination of electron beam lithography (EBL, Raith 150-Two), and reactive ion etching (RIE, SENTECH) has been successfully employed for the uniform production of 3D and 3D PM nano-architectures. As highlighted in **Figure 3a** planar and 3D nanostructures share a common EBL step. A 250 nm polymethyl-methacrylate (PMMA, 950 kDa) layer was spin coated at 3000 rpm for 60 s onto a p-type c-Si (100) wafer. The substrate has been heated at 180 °C for 9 min to get a homogenous PMMA film. After e-beam exposure (electron energy 30 keV and beam current 130 pA), the substrate has been developed in a 3:1 mixture of isopropanol and methyl isobutyl ketone at 4 °C for 3 min. For 2D structures, 3 nm Ti and 18 nm Au were deposited, and the unexposed PMMA removed by ultrasonically assisted lift-off in acetone. In the case of 3D multi-branched nanostar (MBNS) structures (**Figure 3b**), a 20 nm chromium layer was deposited on top of 3 nm Ti and 18 nm Au to act as an etch mask. The excess metal was removed using an ultrasonically assisted lift-off process. Thereafter, substrates were reactive-ion etched (with an etch rate of ≈ 100 nm min⁻¹) in an atmosphere of SF₆ (30 Standard Cubic Centimeters per Minute—SCCM) and C₄F₈ (32 SCCM) at 1 mTorr, where temperature, power and etching time were held at 4°C, 18 W and 25 s, respectively. After the RIE procedure, the chromium layer was removed by wet-etching in a ceric ammonium nitrate-based mixture (Sigma-Aldrich). 3D PM structures (**Figure 3c**) were obtained by depositing 20 nm of chromium after developing the PMMA. Excess chromium has been removed in acetone lift-off, leaving behind multi-branched shape chromium patterns on silicon, serving as etching masks. RIE was employed to produce the underlying pedestals. Subsequently, the chromium mask was removed leaving behind silicon stars on silicon posts. 3 nm Ti and 18 nm Au were evaporated at a deposition rate of 0.3 Å/s in order to form the Au MBNS as well as the perforated film on the underlying substrate.

2.2. Numerical calculations

Finite integration technique FIT (computer simulation technology-microwave, CST-MW) was used to calculate the near-field properties of the MBNS structures while rigorous coupled

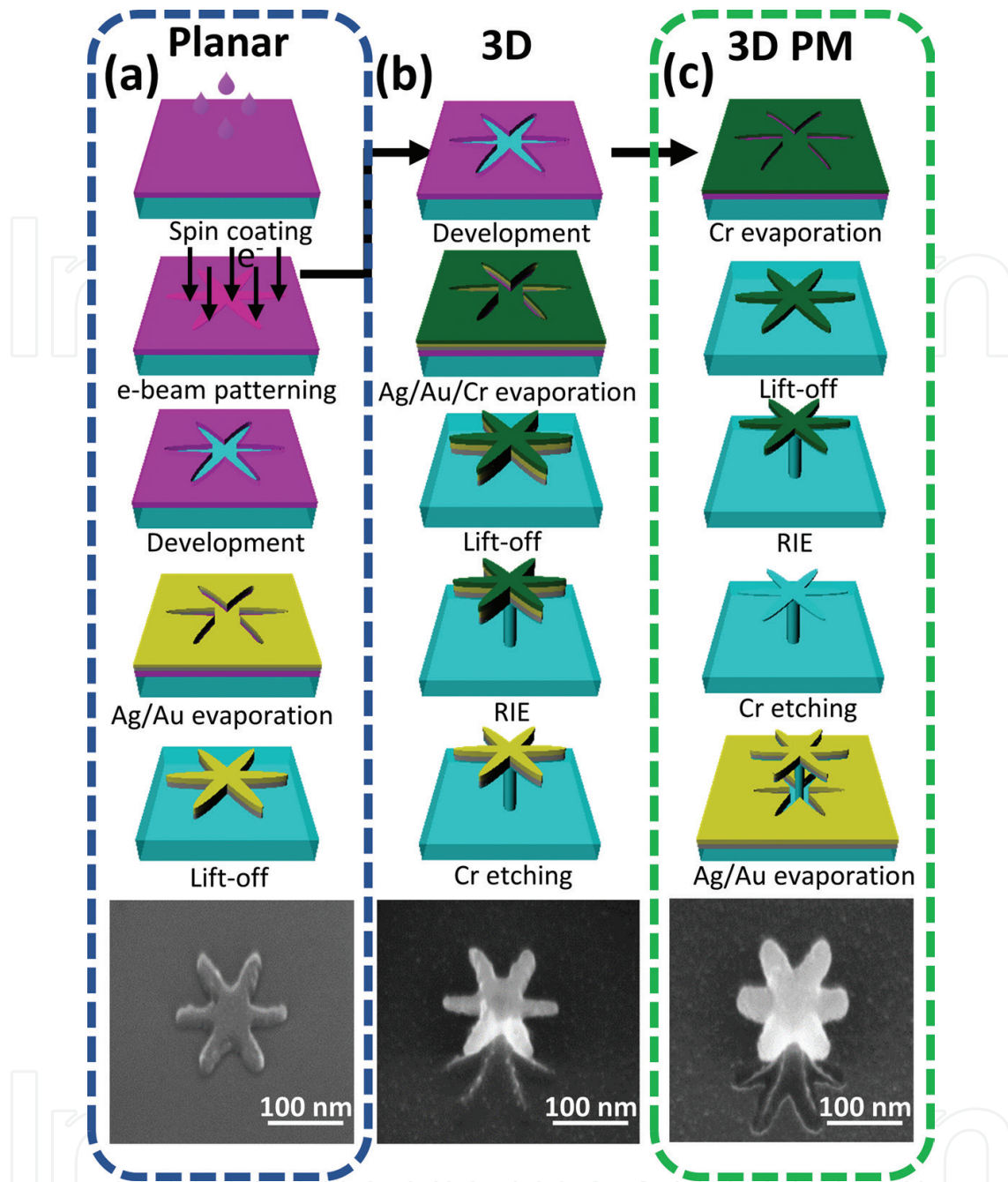


Figure 3. (a–c) Schematic illustration of the protocol, for the fabrication procedure of six-branched nanostructure with different topologies. The corresponding SEM images for six-branched nanostructures are shown below. Reprinted with permission from reference [6]. Copyright 2017 John Wiley and Sons.

wave analysis (Synopsys' Optical Solutions, RSoft) was employed to calculate the far-field response of the nanostructures.

2.3. Optical characterization

The spectral response of the MB nanostructures under normal incidence irradiation was measured using an Olympus IX-73 research microscope. A 100 W halogen lamp (Olympus)

with a broadband illumination source in the visible and near-infrared spectral range has been used. The linearly polarized light was obtained by a Glan-Taylor polarizer. Reflection spectra were measured with a 50× objective of numerical aperture 0.5. The collected light has been acquired through a spectrometer with a Peltier-cooled charge-coupled-device from Ocean Optics (QE65000 and NIRquest512 for visible and near-infrared measurements, respectively).

2.4. Surface-enhanced Raman spectroscopy

SERS spectra were recorded with a Renishaw inVia micro-Raman spectrometer equipped with laser excitations at 830, 785, 633 and 532 nm, and a thermo-electrically cooled charge-coupled device (CCD) as detector. A 150× LEICA HCX PL APO objective (numerical aperture 0.95) was used. The diameter of the laser spot was around 680 nm, 800 nm, 1 μm and 1.07 μm for excitation wavelengths at 532, 633, 785 and 830 nm, respectively. The first order silicon peak at 520 cm⁻¹ was used to calibrate the instrument; all the spectra were recorded at room temperature in the backscattering geometry. Wire 3.0 software was used to correct the baseline with a third-order polynomial fit. The probe molecules, p-aminothiophenol (p-MA) used in this study, were purchased from Sigma-Aldrich.

2.5. Analyte preparation

A stock solution of p-MA at 1 × 10⁻³ M concentration was prepared by dissolving the solid analyte into ethanol. Afterward, 1 × 10⁻⁶ M to 1 × 10⁻¹⁵ M solutions were prepared by further dilution. Molecules were deposited onto the substrate by chemisorption process. The samples were dipped for 20 min and then rinsed in ethanol in order to remove the excess molecules that were not covalently bounded to the metallic surface. Finally, the substrates were dried with nitrogen gas.

3. Results and discussion: engineering 3D MBNS structures

Raman efficiency and SERS signal intensity have been systematically investigated in different plasmonic platforms, elucidating the effect of substrate, IPS, polarization, metal composition, number of branches and geometrical arrangement, on EM near-field localization and enhancement.

3.1. Effect of geometry, IPS and polarization on SERS enhancement

The effect of 2D and 3D geometry on electric field and SERS enhancements was initially studied using five-branched nanostructure dimers with sub-10 nm IPS as a test-bench. **Figure 4a** shows the schematic presentation of the five-branched 3D PM dimer structure, where $L = 150$ nm, $h = 150$ nm, $B_w = 50$ nm and $P_D = 40$ nm denote star size, height, branch width and Si pillar diameter, respectively. The effect of nanostructure height on E-field enhancement is shown in **Figure 4b–d**, where the structure size and IPS were kept constant

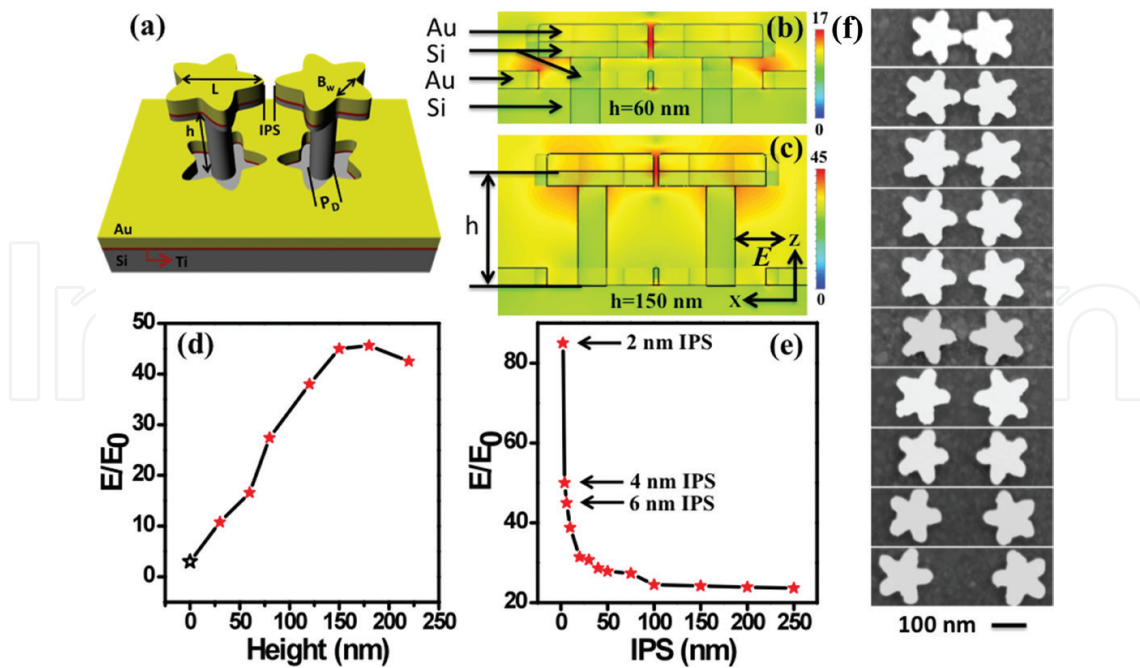


Figure 4. (a) Schematic representation of five-branched 3D PM nanostructure dimer with 150 nm structure size and 6 nm IPS. (b and c) E-field distribution of the nanostructures at $h = 60$ and 150 nm, respectively. The excitation source is set to 830 nm. Calculated E-field enhancement with respect to nanostructure height (d), and as a function of IPS (e). (f) Normal-incidence SEM images of five-branched 3D PM nanostructure dimer with IPS varying from 6 to 200 nm (top to down, respectively). Reprinted with permission from reference [36]. Copyright 2014 John Wiley and Sons.

for all the samples. A low E-field enhancement (E/E_0 , where E and E_0 are the local and the incident electric fields) is observed for the MB nanostructures directly laid on the bulk Si substrate (for $h = 0$ nm), owing to the strong overlapping of the local fields within the high refractive index Si material. For $h = 60$ nm, a $6\times$ improvement of local E-field enhancement compared to the 2D structure is observed due to the reduction of the overlap between local E-fields and Si substrate (Figure 4b). At $h = 150$ nm (Figure 4c), the local E-field enhancement is $15\times$ that of the corresponding nanostructure with “planar” geometry. Thereafter, a slight reduction is observed with a further increase of h . The role of IPS on E-field enhancement is investigated (Figure 4e) with nanostructures of fixed L , h and different IPS ranging from 2 to 250 nm. For IPS of around 2 nm, an E-field enhancement of 85 is observed, and it decreases exponentially with increasing interparticle distances. The large E-fields at low IPS are due to the strong interaction of the LSPRs supported by the nanostructures, thus resulting in the strong localization of intense E-fields (hot-spots). Figure 4f shows the SEM images of the nanostructures with 6 – 200 nm IPS, top-down, respectively.

In order to evaluate the effect of height and IPS experimentally, SERS measurements were performed with p-MA molecules chemisorbed from a solution at $10 \mu\text{M}$ concentration, Figure 5. The incident laser wavelength, power and acquisition time were set to 830 nm, 1.4 mW and 10 s, respectively. The incident light polarization was kept parallel to the IPS axis. Figure 5a shows the SERS spectrum of p-MA molecules on five-branched nanostructure dimers with 150 nm height and 6 nm IPS. Prominent modes of p-MA were clearly visible: strong bands

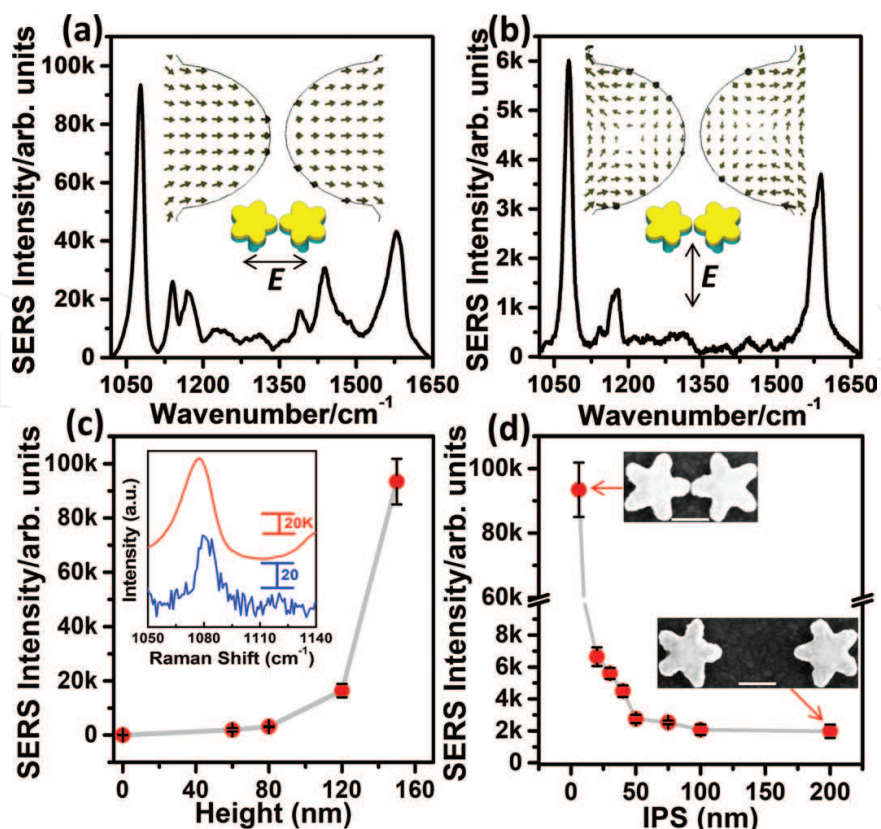


Figure 5. (a and b) Typical SERS spectra of p-MA molecules (chemisorbed at $10 \mu\text{M}$ concentration) on five-branched 3D PM nanostructure dimer with 6 nm IPS. The excited polarization is set parallel (a) and perpendicular (b) to IPS axis. The corresponding calculated surface-charge distribution is represented by direction arrows, shown in the inset. (c) Experimental SERS signal intensity at 1077 cm^{-1} as a function of nanostructure height, where the IPS is fixed at 6 nm. The inset shows the SERS spectra of five-branched nanostructures at $h = 0$ (blue spectrum) and 150 nm (red spectrum). (d) Variation of the SERS signal intensity with respect to IPS with constant h at 150 nm . Reprinted with permission from Ref. [36]. Copyright 2014 John Wiley and Sons.

are centered at 1077 and 1590 cm^{-1} while low-intense bands correspond to 1140 , 1179 , 1390 and 1438 cm^{-1} [6, 8]. Polarization-dependent SERS signal enhancement of MB nanostructures is shown in **Figure 5a** and **b**, where the polarization was set parallel and perpendicular to IPS axis, respectively. Insets represent the calculated surface-charge distributions in correspondence of the IPS region. A dipolar-like distribution of surface charges was observed when the incident light is parallel to the IPS axis (inset of **Figure 5a**). The in-phase dipole moments generate an intense E-field (hot-spot) in the IPS region due to the strong coupling of the sub-10 nm gapped nanostructures. In the case of perpendicular polarization (inset of **Figure 5b**), the effective dipoles are aligned across the interparticle nanocavity leaving a low-intensity local E-field in the IPS region. The corresponding SERS spectra (**Figure 5a** and **b**) discriminate the polarization-induced SERS signal intensities with a factor of 15. The C-S stretching mode located at 1077 cm^{-1} was used to calculate the SERS enhancement factor. **Figure 5c** displays the SERS intensity dependence on nanostructure height of the specific strong band located at 1077 cm^{-1} , showing an exponential-like growth. The inset confirms the high signal-to-noise (SNR) ratio of the 3D PM structures compared to the planar case, for $h = 0$ (blue spectrum) and $h = 150 \text{ nm}$ (red spectrum), respectively. The impact of IPS on SERS signal enhancement

is shown in **Figure 5d**. An exponential increment in the SERS intensity (around 50 \times) has been observed upon reduction of the IPS from 200 nm to 6 nm. The experimental findings, i.e., SERS signal dependence on nanostructure height and interparticle separation, are in good agreement with the numerical calculations reported in **Figure 4d** and **e**.

3.2. Effect of bimetal layer, and recycling of SERS substrates

To evaluate the impact of the metal layer composition on SERS signal enhancement, five-branched nanostructure dimers in a ring structure with Au, Ag and AgAu metal layers were investigated. The schematic representation of the AgAu architecture is presented in **Figure 6a**, while SEM images of the corresponding structure are reported in **Figure 6b–d**. The near-field distribution of Au and AgAu nanostructures has been summarized in **Figure 7a–d**. Due to

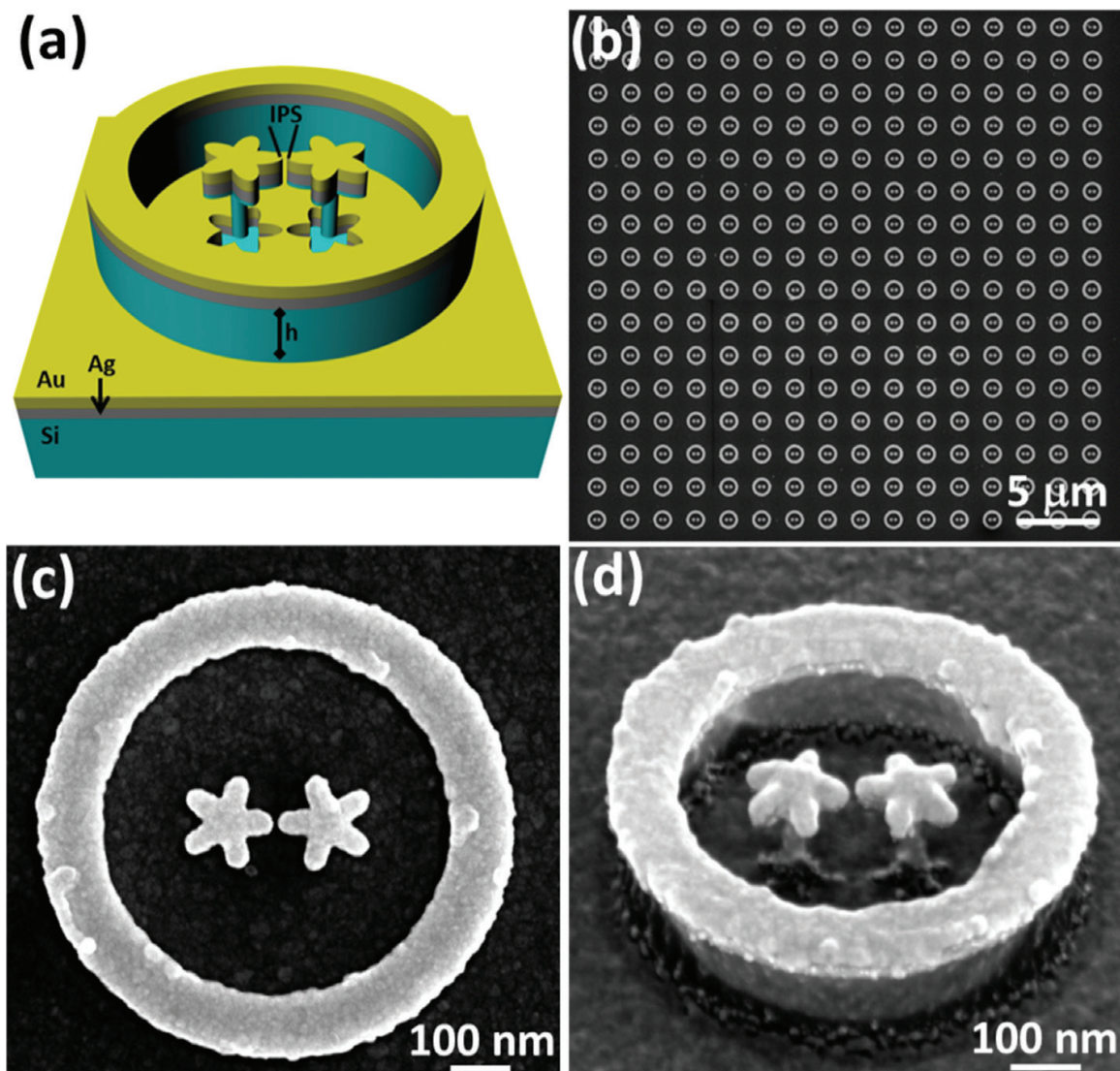


Figure 6. (a) Schematic representation of five-branched 3D PM nanostructure dimer. (b) Normal-incidence SEM image of the nanostructures over a large area. (c and d) Top and tilted view images of individual nanostructures. Reprinted with permission from Ref. [8]. Copyright 2014 American Chemical Society.

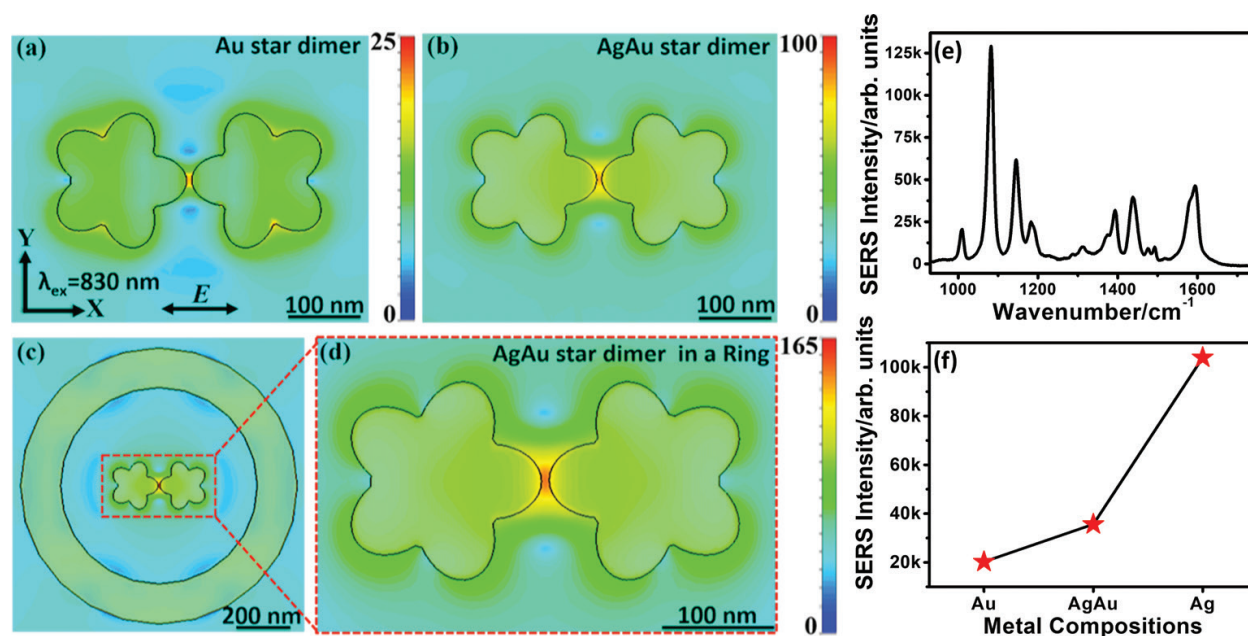


Figure 7. E-field distribution of five-branched 3D PM nanostructure dimer with Au (a) and AgAu (b) metal layers, in the x-y plane. (c and d) E-field distribution of five-branched 3D PM nanostructure dimer in a ring structure with AgAu metal layers. Reprinted with permission from reference [8]. Copyright 2014 American Chemical Society. (e) Typical SERS spectrum of p-MA molecule (at 10 μM concentration) on five-branched 3D PM nanostructure dimer in the ring structure. The exciting laser source, power and accumulation time were set to 830 nm, 1.4 mW and 15 s, respectively. The incident light polarization was set parallel to IPS axis. (f) SERS signal intensity at 1077 cm^{-1} as a function of metal layer compositions.

the strong plasmon resonance of Ag, bimetallic AgAu configurations are endowed with a 4 times higher EM field enhancement. The effect of the nanoring on the MB dimer is shown in **Figure 7c** and **d**. The scattered light is reflected back towards the ring centre where the nanostructures are placed, hence increasing the EM field enhancement in the IPS region by a factor 1.65. **Figure 7e** shows the typical Raman spectrum of p-MA (10 μM concentration) on AgAu five-branched dimers in the ring structure with an IPS of 5 nm. The polarization of the incident light was fixed parallel to the IPS axis. Characteristic Raman bands of p-MA can be clearly observed in the acquired spectrum. The impact of metal layer composition on SERS signal enhancement is plotted for the band located at 1077 cm^{-1} (**Figure 7f**), using 20 nm IPS MB dimer structures with 20 nm Au, 20/20 nm Ag/Au and 20 nm Ag metal layers.

The 3D nanostructure configuration presented so far allows recycling, long-term stability and reutilization of the SERS substrate, thus reducing fabrication costs. **Figure 8a** shows the regeneration protocol for the present architecture. However, as clearly highlighted by the cleaning steps, the process is fully compatible with any kind of 3D plasmonic configuration. In 3D geometry, the nanostructure morphology is conserved by the underlying Si template, while the plasmon active layer is simply recovered by a mask-less wet etching process, followed by metal redeposition. The chemisorbed analyte molecules used for SERS measurements will be completely removed together with the pre-existent metal layer, thus allowing employment of different molecular species after recycling. In order to test the effectiveness of the regeneration process, we have recycled the AgAu nanostructures up to five times (**Figure 8b**) and investigated their SERS response. The corresponding SEM images are shown in the top panel.

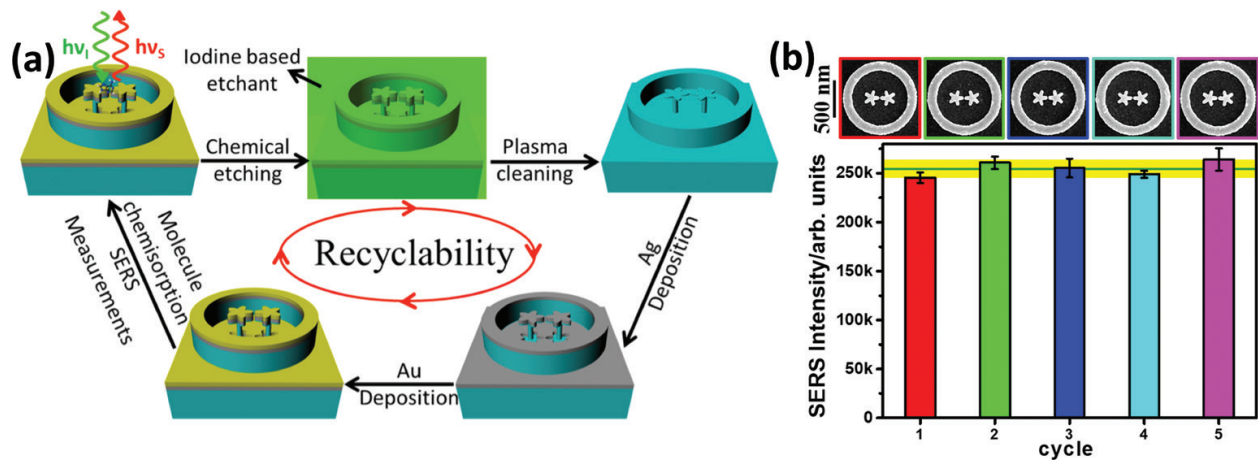


Figure 8. (a) Schematic representation of the maskless recycling process. (b) SERS signal intensity of p-Ma at 1077 cm⁻¹ vs. number of regeneration cycles and corresponding SEM images at each recycling step in the top panel. Reprinted with permission from Ref. [8]. Copyright 2014 American Chemical Society.

The SERS signal intensity of the C–S stretching band of p-MA measured after each regeneration cycle is reported in **Figure 8b**. A good correspondence between different recycling steps is clearly observed, showing an average SERS signal deviation below 10%.

3.3. Effect of branch number, perforated metal layer and overall nanostructure arrangement

So far, we have engineered the five-branched nanostructure dimers to improve the hot-spot intensity as a function of nanostructure height, IPS, incoming light polarization and metal composition. Nevertheless, at very low concentrations (down to the femtomolar scale), the number of molecules available per hot-spot is decreased, and thus it is necessary to endow the nanostructures with high hot-spot densities in order to improve their detection limit. In view of that, single plasmonic nanostructures with multiple branches (4–10) and sharp protrusions (tip radius < 10 nm) were investigated.

The schematic representation of a typical eight-branched bimetallic AgAu nanostructure with 3D PM geometry and 200 nm IPS is shown in **Figure 9a**. Nanostructures with 4–10 branches, 20 nm Ag and 20 nm Au metal layers, 140 nm width, 150 nm high and tip radius of 10 nm were used to investigate the effect of hot-spot density on SERS signal enhancement. Normal-incidence SEM image of eight-branched MB nanostructure is shown in **Figure 9b**, where the inset depicts a 54° tilted view. Besides, normal-incidence SEM images of individual MB structures with 4–10 branches are reported in the bottom panel of **Figure 9b**. A typical reflection spectrum of eight-branched 3D PM nanostructures is shown in **Figure 9c**, where multiple plasmonic resonances are clearly observable. To evaluate the effect of branch number on the LSPRs and hot-spot generation, far-field optical spectra and near-field distribution were calculated using RSoft and CST-MW numerical approaches. Distribution of E-field enhancement (E/E_0) for 4–10 branched 2D nanostructures at their respective LSPRs is shown in **Figure 10a–g**. The corresponding data points are shown in **Figure 10h**, along with their experimental counterparts. The incident polarization is set parallel to the x-axis. In the case of 4 branched nanostructures, two

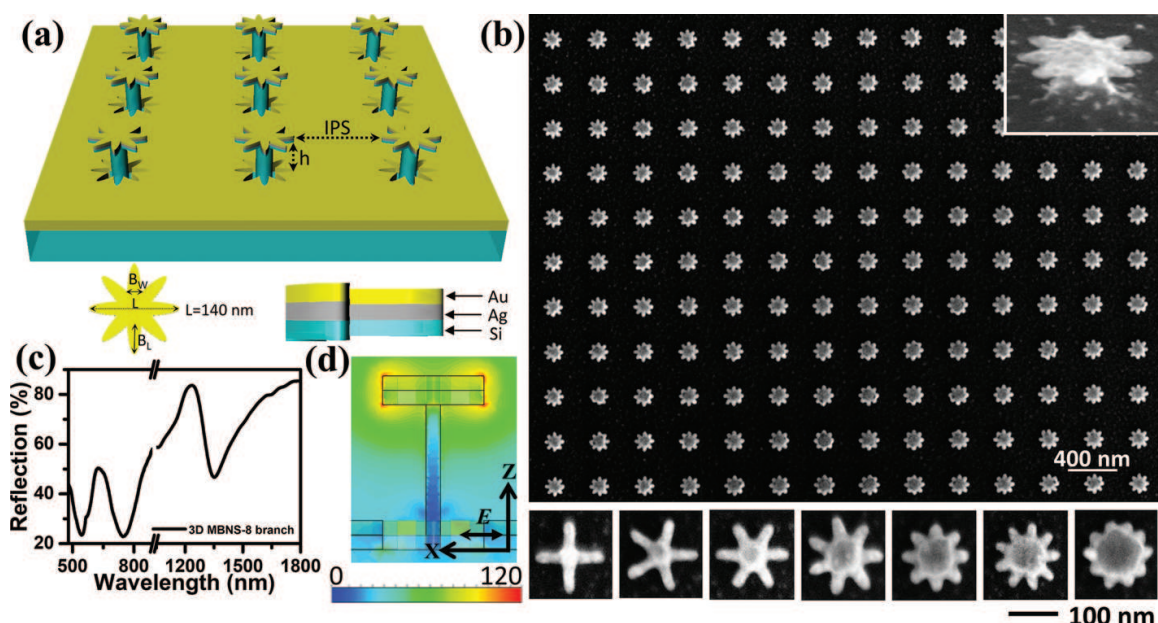


Figure 9. (a) Schematic of bimetallic 3D PM nanostructure for eight-branched nanostructure geometry. (b) Normal incidence SEM image of 3D MB nanostructures with eight-branches arranged in a quadratic array of 200 nm IPS. The inset represents the 54° tilted view of the MBNS with 150 nm silicon pillar height. The bottom panel shows SEM images of MBNS with 4–10 branches, where each micrograph shares the same scale bar. (c) A typical reflection spectrum of eight-branched 3D PM nanostructure. (d) Electric field distribution of eight-branched 3D PM nanostructure at its characteristic LSPR position of 685 nm.

hot-spots are observed parallel to the incident light polarization direction. The hot-spots density increases according to the number of branches, inducing a clear blue shift in LSPR spectral position (**Figure 10h**). This behaviour can be explained using a simple dipole theory. An increasing hot-spot density, that goes along with the number of branches, results in a higher total restoring force which blue shifts the nanostructure LSPR. Tailoring of the branch morphology enables precise control over the generation and spatial distribution of the hot-spots on the single nanostructure, thus opening new perspectives in reproducible SERS signal detection from large biomolecules, where the analyte size is many times larger than the individual hot-spot volume.

The influence of 2D, 3D and 3D PM geometries on the optical response and SERS enhancement was experimentally validated, as reported in **Figures 11** and **12**, respectively. Numerically calculated reflectance spectra of the eight-branched nanostructures with 2D, 3D and 3D PM topologies (see schematics in **Figure 11b–d**) are shown in **Figure 11a**. The corresponding experimental spectra are summarized in **Figure 11e**. In both cases, the optical spectra are normalized with respect to the flat/unpatterned area of the same sample. The experimental spectra show good correlation with their numerical counterparts. The E-field distribution of the nanostructures at their LSPR position is shown in **Figure 11f–h**. In the 2D case, near-field distribution maps (**Figure 11f**) clearly show the E-field confinement at the metal and bulk silicon interface. Due to the overlap of the E-field profiles into the bulk silicon a low-intense E-field enhancement (around 20) is observed. In general, surface plasmon resonances are tightly confined in high refractive index materials (e.g. silicon), which results in low E-field enhancement, low extinction-cross section, large propagation losses, broadening and red shifting of resonances compared to low-index materials [47]. As highlighted in the previous sections, 3D nanostructures decouple the hot-spot confinement from the substrate and enhance its strength by reducing the effective refractive

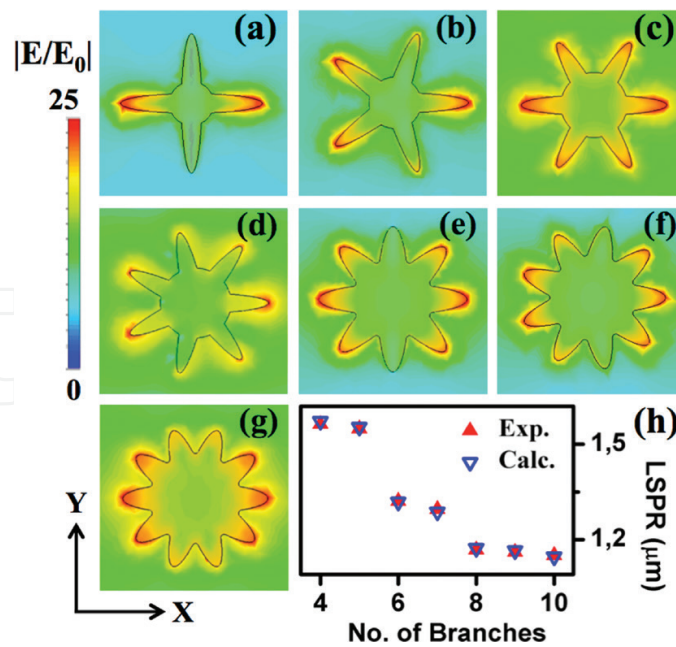


Figure 10. (a–g) E-field distribution of 2D nanostructures with varying branch number (4–10). (h) Corresponding LSPR positions for experimental and calculated data points. Reprinted with permission from Ref. [6]. Copyright 2017 John Wiley & Sons.

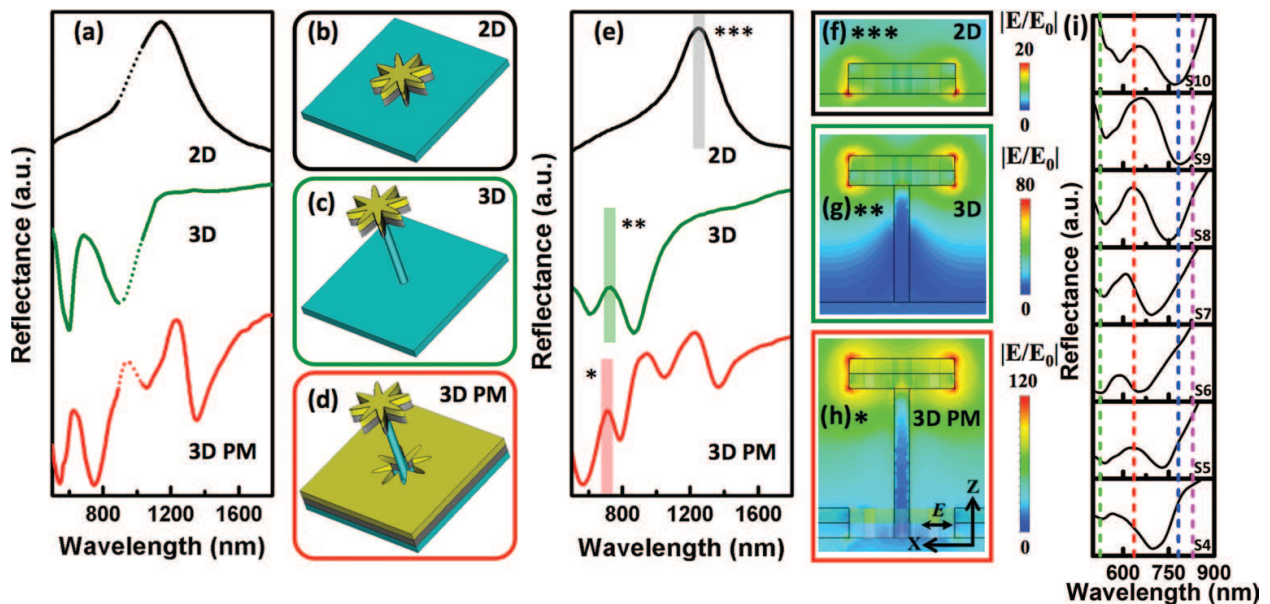


Figure 11. (a) Experimental reflectance spectra of eight-branched nanostructures with 2D, 3D and 3D PM geometries. (b–d) Schematic representations of the structure geometries simulated in (a). (e) Experimentally measured reflection spectra of the nanostructures shown in (a). (f–h). Near-field profiles of E-field distribution in x–z plane for the LSPRs of the nanostructures with 2D, 3D and 3D PM topologies. Reprinted with permission from Ref. [6]. Copyright 2017 John Wiley & Sons.

index of the embedding medium. The reflectance spectrum of the 3D nanostructure (**Figure 11a**) shows a significant blue shift of LSPR (around 485 nm), with a resonance maximum at around 680 nm. **Figure 11g** clearly shows that the generated E-fields (with an enhancement of around 80) are decoupled from the substrate by means of a dielectric nanopedestal. These strong E-field

regions can be easily accessible to the analytes in Raman measurements if compared to the planar configuration. In the case of 3D PM geometry, the numerical spectrum (**Figure 11a**) shows various modes corresponding to the LSPR of the nanostructure and the underlying nanohole, and surface plasmon polaritons (SPP) at metal/air and metal/substrate interfaces. The LSPR position of the 3D PM structure (650 nm) is slightly shifted (a blue shift of 30 nm) from the 3D geometry, and a high E-field enhancement of 120 is observed. A deeper analysis of the perforated metal contribution has been discussed elsewhere [6]. The spectral features corresponding to the LSPRs of the 3D PM nanostructure and star-shaped hole cavity are located at about 620 and 1350 nm, while the 543 and 1050 nm resonances can be associated to the SPPs of the PM layer.

In order to assess the impact of hot-spot density on SERS enhancement, Raman measurements were performed on 4–10 branched nanostructures with p-MA molecules chemisorbed at 1 μM concentration. Typical SERS spectra of 8 branched nanostructures with 2D, 3D and 3D PM geometries are shown above. The incident laser wavelength, acquisition time and power were set to 785 nm, 30 s and 1 mW, respectively, and the incident light polarization was fixed along the x-axis. Characteristic Raman modes of p-MA are clearly visible in the spectra acquired on 3D PM MB nanostructures. In the planar case, the peaks centered around 1077 and 1590 cm^{-1} are experimentally observable, but the other bands are buried into the background noise. When the nanostructures are decoupled from the substrate via a dielectric nanopedestal (3D case), a significant rise in SERS signal intensity is observed along with the presence of all characteristic p-MA Raman modes. Furthermore, an additional enhancement in SERS signal intensity is observed for the 3D PM nanostructure geometry due to the coupling of the MBNS with the reflected light coming from the perforated metal layer underneath. The 3D PM MB nanostructure shows an absolute SERS enhancement in the order of 10^{11} obtained from the evaluation of the peak intensity at 1077 cm^{-1} , with reference to Raman spectra of p-MA molecules on a planar SERS active gold film. Details on the corresponding calculations can be found in [6].

In order to understand the wavelength-dependent hot-spot generation and SERS enhancement, 4–10 branched 3D PM nanostructures were excited with four different laser sources (**Figure 12b**). The SERS signal intensity of the 1077 cm^{-1} band is plotted with respect to the number of branches and excitation lasers (532, 633, 785 and 830 nm). Due to different spectral power densities of the excited lasers, the SERS intensities are normalized independently with respect to the highest peak intensity obtained in the series. A monotonic increment of the SERS signal is observed by raising the number of branches for both 785 and 830 nm laser excitations, which are off-resonance with respect to the nanostructure LSPRs (see, **Figure 11i**). In this scenario, the SERS signal intensity can be associated to the increment of the number of hot-spots with multiple branches. For 633 nm laser excitation, the eight-branched nanostructure shows highest SERS signal intensity owing to the overlap between the LSPR and the laser source. A similar trend has been observed for 532 nm excitation source.

Ultra-sensitive detection of analyte molecules was probed on eight-branched 3D PM nanostructures with p-MA molecules at concentrations ranging from 1 μM to 1 fM (**Figure 12c**). The incident wavelength, power and acquisition time were set to 785 nm, 1 mW and 3 s, respectively. At 1 μM concentration, the SERS spectra show the characteristic Raman bands of p-MA with good SNR. A decrease in SERS signal intensity is observed upon reduction of the molecular concentration from 1 μM to 1 fM, due to a lower number of adsorbed molecules on the nanostructure

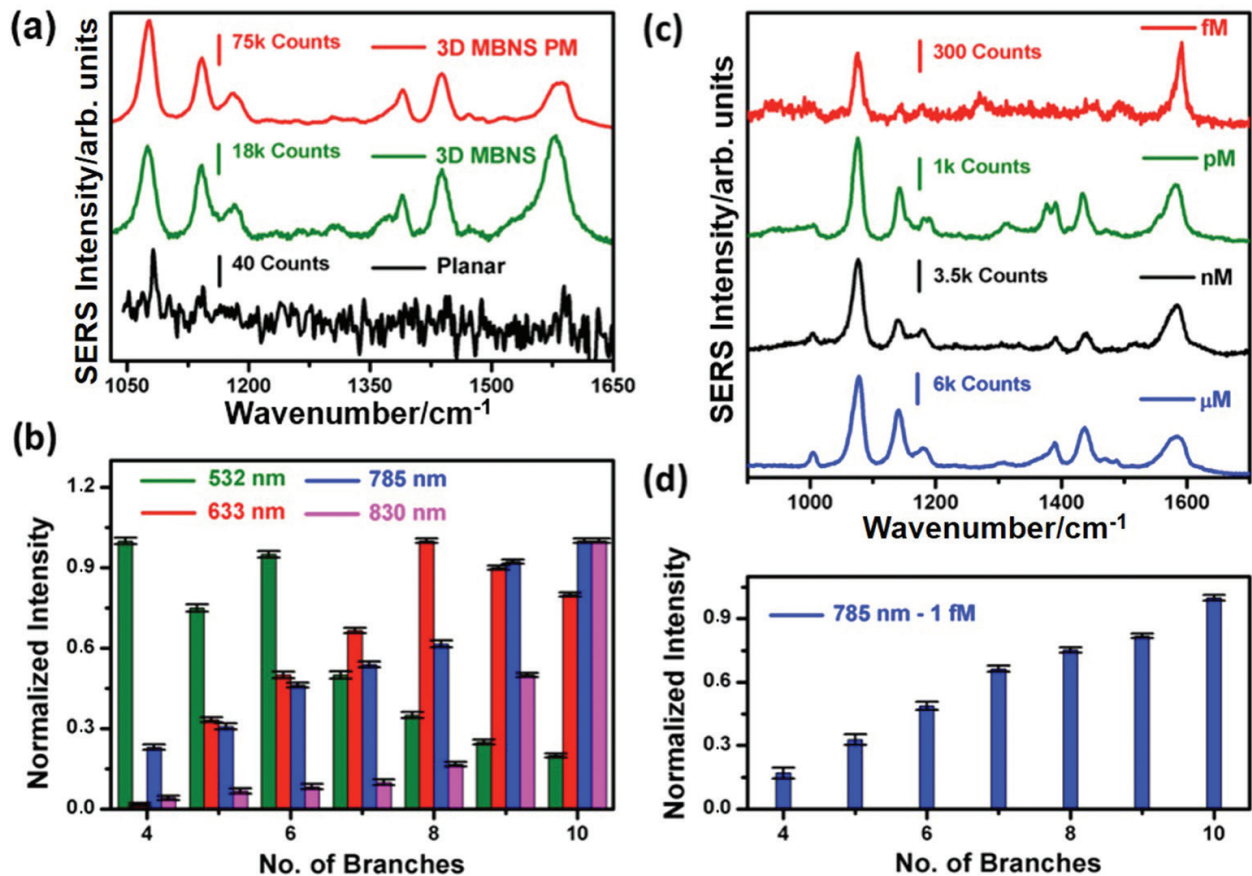


Figure 12. (a) SERS spectra of p-MA molecules chemisorbed at 1 μM concentration on eight-branched nanostructures with 2D, 3D and 3D PM geometries. (b) SERS signal intensity at 1077 cm^{-1} as a function of a number of branches and different exciting wavelengths (532, 633, 785 and 830 nm). (c) SERS spectra of p-MA molecules at 1 μM , 1 nM, 1 pM and 1 fM concentrations taken on eight-branched 3D PM nanostructures for 785 nm laser excitation. (d) SERS signal intensity at 1077 cm^{-1} versus number of branches at ultra-low concentration, 1 fM. Reprinted with permission from Ref. [6]. Copyright 2017 John Wiley & Sons.

surface. For 1 fM concentration, only the Raman bands at 1077 and 1590 cm^{-1} are clearly visible, while the other features lie in the background noise. Despite of this, analyte detection at 1 fM showed the ultra-sensing capability of the substrate towards single/few molecules detection. In order to assess the effect of branch number on the detection limit, SERS measurements were performed on 4–10 branched 3D PM nanostructures with p-MA chemisorbed from a 1 fM concentrated solution (**Figure 12d**). An increment in SERS signal intensity at 1077 cm^{-1} is observed by raising the number of branches, owing to the larger number of generated hot-spots.

Reproducible identification and detection of biological samples/chemicals at ultra-low concentrations remains a huge challenge due to lack of high hot-spot density substrates. At ultra-low concentrations, single/few molecules adsorbed in the vicinity of the hot-spot sites provide the majority of the SERS signal intensity. In this situation, if the molecules are not absorbed in the proximity of the hot-spot, the molecular fingerprint of the analyte cannot be identified. Thus, development of plasmonic nanostructures with a high hot-spot density that enables reproducible detection at ultra-low concentrations is of paramount importance in the field of molecular sensing. Multi-branched nanostructure designs hold concrete promises in this

direction. In view of that, eight-branched 3D PM nanostructures arranged in the form of single, dimer, 3×3 array of clusters and chain of nanostructures, as shown in **Figure 13**, were investigated by keeping the interparticle distance fixed at 200 nm.

Near-field distributions of 2D single, dimer, 3×3 periodic array and chain of eight-branched nanostructures at their characteristic LSPRs, are shown in the **Figure 14a–d**, respectively. In order to reduce the computational time, 2D structures were used to compare the hot-spot density and E-field enhancement. The corresponding LSPR positions (experimental and calculated) are shown in **Figure 15**. A red-shift in the plasmon resonance has been observed with different layouts, as a consequence of the interaction between adjacent nanostructures. It is clearly visible that the hot-spot density is increased with respect to the arrangement schemes and, the highest E-field enhancement is observed for nanostructures arranged in the form of a chain.

SERS spectra were acquired in order to address the effect of different geometrical configurations on the measured signal. **Figure 16a** shows a typical SERS spectrum of p-MA (at $1 \mu\text{M}$ concentration) on eight-branched 3D PM structures arranged in the form of a chain. The exciting laser, acquisition time and power were set to 785 nm, 10 s and 1 mW, respectively, while the impinging light polarization was fixed along the x-axis. **Figure 16b** shows the SERS signal intensity for the band at 1077 cm^{-1} with respect to the nanostructure arrangement. Dimer configuration presents higher field enhancement in comparison to the isolated geometry, as

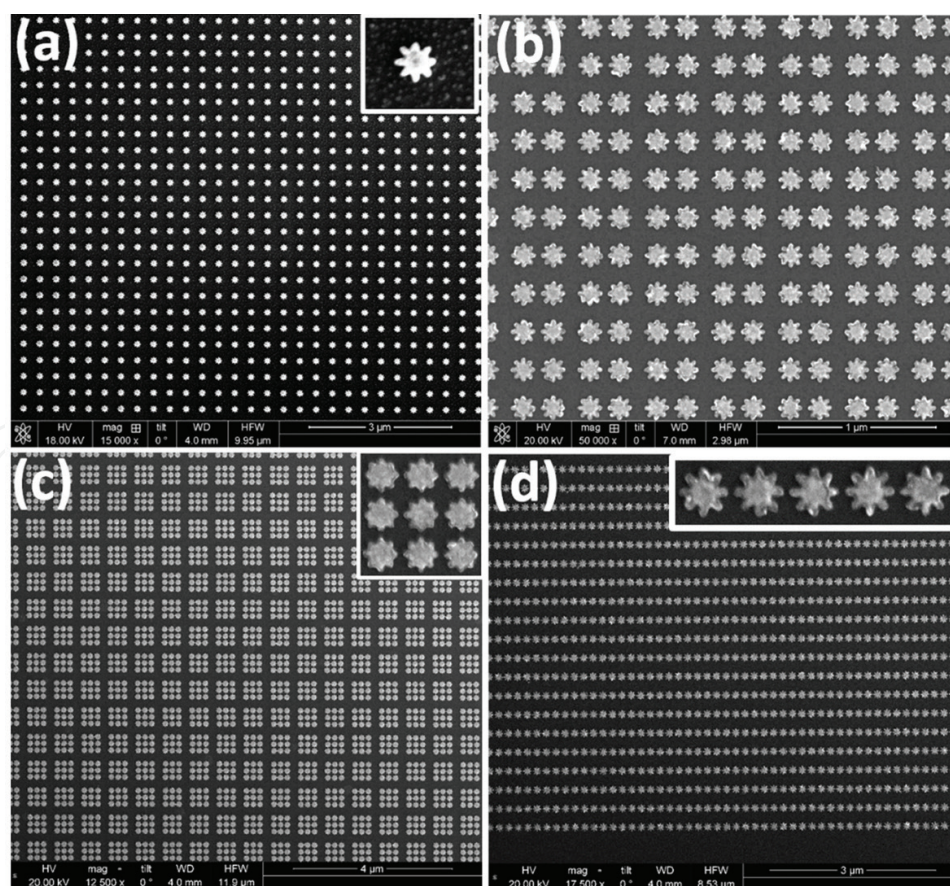


Figure 13. (a–d). Normal incidence SEM images of the eight-branched 3D PM MB nanostructures in the form of single, dimer, 3×3 periodic array of clusters and chain of nanostructures, respectively. The inset shows the magnified view of the nanostructures.

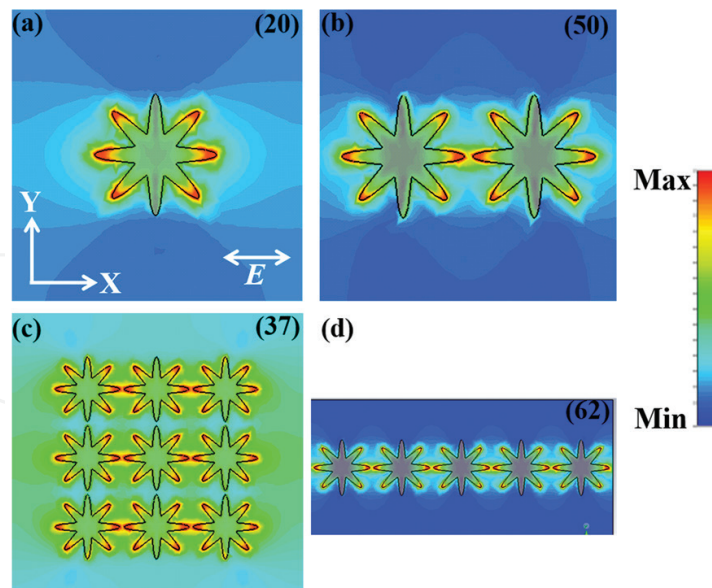


Figure 14. E-field distribution of single, dimer, 3×3 periodic array and chain of MBNS (a–d) at their characteristic LSPRs. The incident light is polarized along the x-axis.

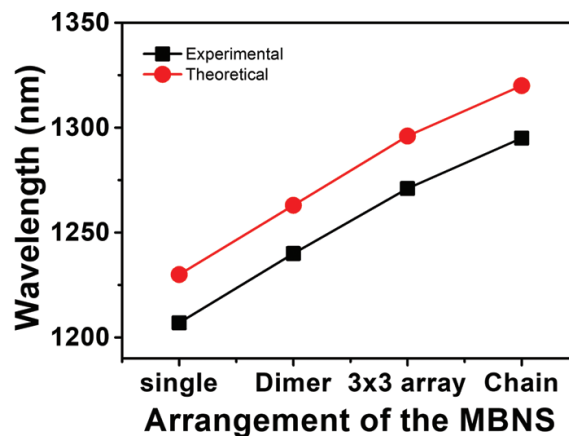


Figure 15. LSPR positions (theoretical and experimental) of 2D eight-branched nanostructures arranged in the form of single, dimer, 3×3 periodic array of clusters and chain of nanostructures.

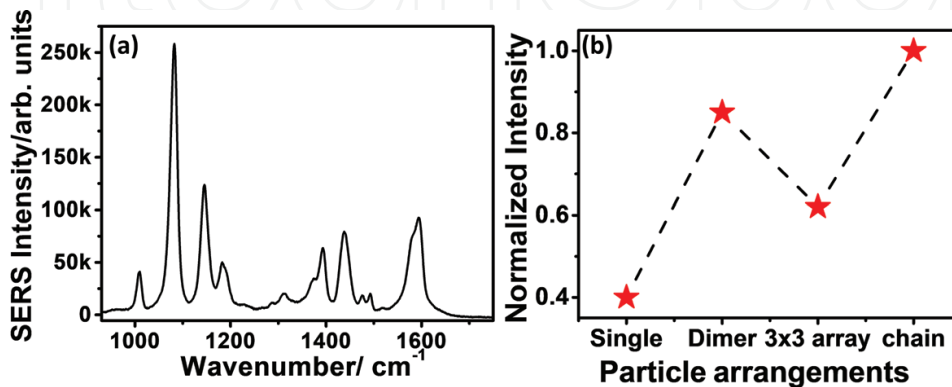


Figure 16. (a) The SERS spectrum of p-MA at $1 \mu\text{M}$ concentration taken on eight-branched 3D PM nanostructures arranged in the form of a chain. (b) Normalized SERS signal intensity variation at 1077 cm^{-1} with respect to different arrangements of the nanostructures at $1 \mu\text{M}$ p-MA concentration.

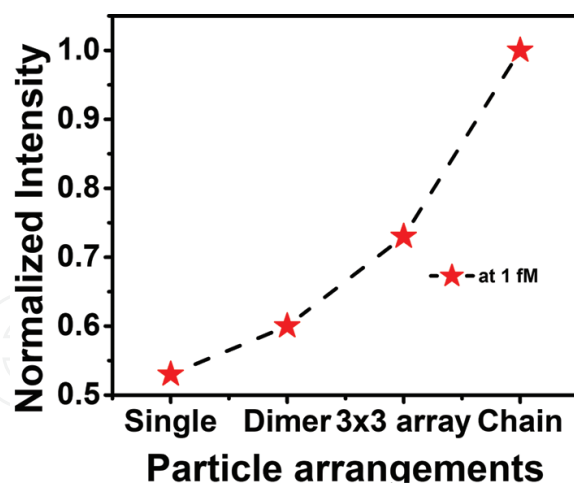


Figure 17. Normalized SERS signal intensity variation at 1077 cm^{-1} with respect to different arrangements of the eight-branched 3D PM nanostructures at 1 fM p-MA concentration.

a consequence of the strong hot-spot confined in the IPS region. Periodic 3×3 arrays of nanostructures show higher E-field enhancement compared to single nanostructures, and a lower E-field enhancement with respect to the dimer layout, which is in good agreement with the E-field enhancements observed in **Figure 14**. Nanostructures arranged in the form of chain show the highest E-field enhancement (a factor of 62) in comparison to the other geometries. **Figure 17** shows the SERS signal intensity at 1077 cm^{-1} as a function of the arrangements of nanostructures at 1 fM p-MA concentration. As in the previous situation, the highest SERS intensities were observed for chains, as a result of the higher hot-spot density.

4. Conclusions and outlook

In summary, the engineering of 3D multi-branched (up to 10 branches) nanostructures for sensing of analyte molecules at ultra-low concentrations, down to 1 fM , is demonstrated to be highly feasible. Numerical simulations were performed to understand the underlying physics of high electric field enhancement of the plasmonic nanostructures. The advancement of the 3D fabrication methods enables the realization of uniform, homogenous and reproducible SERS devices. Reflection and SERS measurements were carried out to evaluate the MB nanostructure performances. Within this context, we demonstrated the importance of the geometry, IPS and polarization on SERS signal enhancement using 3D five-branched nano-star dimers (with sub- 10 nm IPS). The elevated 3D geometry shows the advantage of high E-field enhancement over 2D geometry due to decoupling from the underlying substrate of the strong optical-near fields localized at the metal/dielectric interface. In particular, the 3D geometry enables direct interaction of analytes with hot-spot spatial regions, which are severely affected by solid dielectric substrates in the 2D geometry case. This kind of SERS architectures is particularly important in miniaturized lab-on-chip Raman detection systems, thus allowing the exploitation of lower laser powers with no consequence over the device sensitivity. Moreover, the low-cost recycling capability of the 3D geometry counterbalances the production cost and time defined by the lithographic process. The effect of metal layer composition on SERS signal enhancement of p-MA molecules, and recycling capabilities of

3D structures were investigated with five-branched nanostar dimers in the ring structures. The effect of the number of branches, varying from 4 to 10, on the hot-spot generation and SERS enhancement was evaluated by using individual nanostructures (separated by 200 nm IPS). Moreover, the arrangement of MB nanostructures in various configurations (single, dimer, 3×3 array of clusters and chain of nanostructures) was evaluated to improve the device detection limit towards the single-molecule regime. 3D multi-branched nanostructures exhibit enhancement factors in the order of 10^{11} with an extremely high sensing capability (down to 1fM concentration). In this view, engineering the aforementioned architectures for high hot-spot density paves the way towards commercial biosensing applications, which require single/few-molecule detection sensitivity, with scalable manufacturing methods and cost-effective approaches. The proposed devices do not require specific labeling of the investigated analytes and multiple testing can be evaluated on the same platform. A new class of biological experiments will be therefore feasible, including monitoring growth factors that are produced from cultured cells. Moreover, our plasmonic nanostructures can be employed for direct detection of proteins within biological samples and real-time monitoring of chemical reactions. When applied to biomedicine, the present results, combined with already available purification methods, suggest the possibility of improving the early detection of several diseases, including cancer, where the number of clinically significant molecules at the onset of the pathology is very small and often generated by a single cell.

Author details

Anisha Chirumamilla^{1,2}, Manohar Chirumamilla^{2*}, Alexander S. Roberts³, Andrea Cerea⁴, Esben Skovsen², Francesco De Angelis⁴, Remo Proietti Zaccaria^{4,5}, Peter Kjær Kristensen², Roman Krahne⁴, Duncan S. Sutherland¹, Sergey I. Bozhevolnyi³, Kjeld Pedersen² and Andrea Toma^{4*}

*Address all correspondence to: mch@nano.aau.dk and andrea.toma@iit.it

1 Interdisciplinary Nanoscience Center (iNANO), Århus University, Aarhus C, Denmark

2 Department of Physics and Nanotechnology, Aalborg University, Aalborg Øst, Denmark

3 Centre for Nano Optics, University of Southern Denmark, Odense M, Denmark

4 Istituto Italiano di Tecnologia, Genova, Italy

5 Cixi Institute of Biomedical Engineering, Ningbo Institute of Materials Technology and Engineering, Chinese Academy of Sciences, Ningbo, China

References

- [1] Cao Y, Zhang J, Yang Y, Huang Z, Long NV, Fu C. Engineering of SERS substrates based on noble metal nanomaterials for chemical and biomedical applications. *Applied Spectroscopy Reviews*. 2015;**50**:499. DOI: 10.1080/05704928.2014.923901

- [2] Xuming Z, Yu Lim C, Ru-Shi L, Din Ping T. Plasmonic photocatalysis. *Reports on Progress in Physics*. 2013;**76**:046401
- [3] Lane LA, Qian X, Nie S. SERS nanoparticles in medicine: From label-free detection to spectroscopic tagging. *Chemical Reviews*. 2015;**115**:10489. DOI: 10.1021/acs.chemrev.5b00265
- [4] Fateixa S, Nogueira HIS, Trindade T. Hybrid nanostructures for SERS: Materials development and chemical detection. *Physical Chemistry Chemical Physics*. 2015;**17**:21046. DOI: 10.1039/C5CP01032B
- [5] Huang J-A, Zhang Y-L, Ding H, Sun H-B. SERS-enabled lab-on-a-chip systems. *Advanced Optical Materials*. 2015;**3**:618. DOI: 10.1002/adom.201400534
- [6] Chirumamilla M, Chirumamilla A, Roberts AS, Proietti Zaccaria R, De Angelis F, Kjær Kristensen P, Krahn R, Bozhevolnyi SI, Pedersen K, Toma A. Hot-spot engineering in 3D multi-branched nanostructures: Ultrasensitive substrates for surface-enhanced Raman spectroscopy. *Advanced Optical Materials*. 2017;**5**:1600836. DOI: 10.1002/adom.201600836
- [7] Chirumamilla M, Chirumamilla A, Yang Y, Roberts AS, Kristensen PK, Chaudhuri K, Boltasseva A, Sutherland DS, Bozhevolnyi SI, Pedersen K. Large-area Ultrabroadband absorber for solar thermophotovoltaics based on 3D titanium nitride nanopillars. *Advanced Optical Materials*. 2017;**5**:1700552. DOI: 10.1002/adom.201700552
- [8] Gopalakrishnan A, Chirumamilla M, De Angelis F, Toma A, Proietti Zaccaria R, Krahn R. Bimetallic 3D nanostar dimers in ring cavities: Recyclable and robust surface-enhanced Raman scattering substrates for signal detection from few molecules. *ACS Nano*. 2014;**8**:7986. DOI: 10.1021/nn5020038
- [9] Willets KA, Duyne RPV. Localized surface Plasmon resonance spectroscopy and sensing. *Annual Review of Physical Chemistry*. 2007;**58**:267. DOI: 10.1146/annurev.physchem.58.032806.104607
- [10] Kelly KL, Coronado E, Zhao LL, Schatz GC. The optical properties of metal nanoparticles: The influence of size, shape, and dielectric environment. *The Journal of Physical Chemistry B*. 2002;**107**:668. DOI: 10.1021/jp026731y
- [11] Moskovits M. Imaging: Spot the hotspot. *Nature*. 2011;**469**:307
- [12] Zhang R, Zhang Y, Dong ZC, Jiang S, Zhang C, Chen LG, Zhang L, Liao Y, Aizpurua J, Luo Y, Yang JL, Hou JG. Chemical mapping of a single molecule by plasmon-enhanced Raman scattering. *Nature*. 2013;**498**:82. DOI: 10.1038/nature12151
- [13] Ahmed A, Gordon R. Single molecule directivity enhanced Raman scattering using nanoantennas. *Nano Letters*. 2012;**12**:2625. DOI: 10.1021/nl301029e
- [14] Radziuk D, Moehwald H. Prospects for plasmonic hot spots in single molecule SERS towards the chemical imaging of live cells. *Physical Chemistry Chemical Physics*. 2015;**17**:21072. DOI: 10.1039/C4CP04946B

- [15] Das G, Chirumamilla M, Toma A, Gopalakrishnan A, Proietti Zaccaria R, Alabastri A, Leoncini M, Di Fabrizio E. Plasmon based biosensor for distinguishing different peptides mutation states. *Scientific Reports*. 2013;**3**:1-6. DOI: 10.1038/srep01792
- [16] Toma A, Das G, Chirumamilla M, Saeed A, Proietti Zaccaria R, Razzari L, Leoncini M, Liberale C, De Angelis F, Di Fabrizio E. Fabrication and characterization of a nanoantenna-based Raman device for ultrasensitive spectroscopic applications. *Microelectronic Engineering*. 2012;**98**:424. DOI: 10.1016/j.mee.2012.07.066
- [17] Das G, Chirumamilla M, Gopalakrishnan A, Toma A, Panaro S, Proietti Zaccaria R, De Angelis F, Di Fabrizio E. Plasmonic nanostars for SERS application. *Microelectronic Engineering*. 2013;**111**:247. DOI: 10.1016/j.mee.2013.04.028
- [18] Chirumamilla M, Das G, Toma A, Gopalakrishnan A, Proietti Zaccaria R, Liberale C, De Angelis F, Di Fabrizio E. Optimization and characterization of au cuboid nanostructures as a SERS device for sensing applications. *Microelectronic Engineering*. 2012;**97**:189. DOI: 10.1016/j.mee.2012.05.004
- [19] Hanif M, Juluri RR, Chirumamilla M, Popok VN. Poly(methyl methacrylate) composites with size-selected silver nanoparticles fabricated using cluster beam technique. *Journal of Polymer Science Part B: Polymer Physics*. 2016;**54**:1152. DOI: 10.1002/polb.24021
- [20] Accardo A, Proietti Zaccaria R, Candeloro P, Gentile F, Coluccio ML, Das G, Krahn R, Liberale C, Toma A, Panaro S, Miele E, Chirumamilla M, Rajamanickam V, Di Fabrizio E. In: Bhushan B, Luo D, Schrick SR, Sigmund W, Zauscher S, editors. *Handbook of Nanomaterials Properties*. Heidelberg: Springer; 2014. p. 615. DOI: 10.1007/978-3-642-31107-9_42
- [21] Toma A, Das G, Proietti Zaccaria R, Chirumamilla M, Gentile F, Mearini F, Coluccio ML, Leoncini M, Liberale C, Francardi M, De Angelis F, Di Fabrizio E. In: Lamy de la Chapelle M, Pucci A, editors. *Nanoantenna: Plasmon-Enhanced Spectroscopies for Biotechnological Applications*. USA: Pan Stanford; 2013. p. 267. DOI: 10.1201/b14594-9
- [22] Wang ZY, Zhang RJ, Wang SY, Lu M, Chen X, Zheng YX, Chen LY, Ye Z, Wang CZ, Ho KM. Broadband optical absorption by tunable Mie resonances in silicon nanocone arrays. *Scientific Reports*. 2015;**5**:7810. DOI: 10.1038/srep07810
- [23] Wei H, Hossein Abtahi SM, Vikesland PJ. Plasmonic colorimetric and SERS sensors for environmental analysis. *Environmental Science: Nano*. 2015;**2**:120. DOI: 10.1039/C4EN00211C
- [24] Roberts AS, Søndergaard T, Chirumamilla M, Pors A, Beermann J, Pedersen K, Bozhevolnyi SI. Light extinction and scattering from individual and arrayed high-aspect-ratio trenches in metals. *Physical Review B*. 2016;**93**:075413. DOI: 10.1103/PhysRevB.93.075413
- [25] Nie S, Emory SR. Probing single molecules and single nanoparticles by surface-enhanced Raman scattering. *Science*. 1997;**275**:1102. DOI: 10.1126/science.275.5303.1102
- [26] Proietti Zaccaria RSP, Toma A, Chirumamilla M, Giugni A, Das G, Krahn R, Di Fabrizio E. In: Lamy de la Chapelle M, Giuseppe Gucciardi P, Lidgi-Guigui N, editors. *Handbook of Enhanced Spectroscopy*. USA: Pan Stanford; 2015. p. 141. DOI: 10.4032/9789814613330

- [27] Etchegoin PG, Le Ru EC. A perspective on single molecule SERS: Current status and future challenges. *Physical Chemistry Chemical Physics*. 2008;**10**:6079. DOI: 10.1039/b809196j
- [28] Harmsen S, Huang R, Wall MA, Karabeber H, Samii JM, Spaliviero M, White JR, Monette S, O'Connor R, Pitter KL, Sastra SA, Saborowski M, Holland EC, Singer S, Olive KP, Lowe SW, Blasberg RG, Kircher MF. Surface-enhanced resonance Raman scattering nanostars for high-precision cancer imaging. *Science Translational Medicine*. 2015;**7**:271ra7. DOI: 10.1126/scitranslmed.3010633
- [29] Alvarez-Puebla RA, Liz-Marzán LM. SERS-based diagnosis and biodetection. *Small*. 2010;**6**:604. DOI: 10.1002/smll.200901820
- [30] Lin C-C, Yang Y-M, Chen Y-F, Yang T-S, Chang H-C. A new protein A assay based on Raman reporter labeled immunogold nanoparticles. *Biosensors and Bioelectronics*. 2008;**24**:178. DOI: 10.1016/j.bios.2008.03.035
- [31] Lee S, Kim S, Choo J, Shin SY, Lee YH, Choi HY, Ha S, Kang K, Oh CH. Biological imaging of HEK293 cells expressing PLC γ 1 using surface-enhanced Raman microscopy. *Analytical Chemistry*. 2007;**79**:916. DOI: 10.1021/ac061246a
- [32] Kneipp K, Wang Y, Kneipp H, Perelman LT, Itzkan I, Dasari RR, Feld MS. Single molecule detection using surface-enhanced Raman scattering (SERS). *Physical Review Letters*. 1997;**78**:1667. DOI: 10.1103/PhysRevLett.78.1667
- [33] Reilly TH, Chang S-H, Corbman JD, Schatz GC, Rowlen KL. Quantitative evaluation of plasmon enhanced Raman scattering from nanoaperture arrays. *The Journal of Physical Chemistry C*. 2007;**111**:1689. DOI: 10.1021/jp066802j
- [34] Xu H, Bjerneld EJ, Käll M, Börjesson L. Spectroscopy of single Hemoglobin molecules by surface enhanced Raman scattering. *Physical Review Letters*. 1999;**83**:4357. DOI: 10.1103/PhysRevLett.83.4357
- [35] Rodríguez-Lorenzo L, Álvarez-Puebla RA, Pastoriza-Santos I, Mazzucco S, Stéphan O, Kociak M, Liz-Marzán LM, García de Abajo FJ. Zeptomol detection through controlled ultrasensitive surface-enhanced Raman scattering. *Journal of the American Chemical Society*. 2009;**131**:4616. DOI: 10.1021/ja809418t
- [36] Chirumamilla M, Toma A, Gopalakrishnan A, Das G, Proietti Zaccaria R, Krahn R, Rondanina E, Leoncini M, Liberale C, De Angelis F, Di Fabrizio E. 3D nanostar dimers with a sub-10-nm gap for single-/few-molecule surface-enhanced Raman scattering. *Advanced Materials*. 2014;**26**:2353. DOI: 10.1002/adma.201304553
- [37] Di Fabrizio E, Gentile F, Donnorso MP, Chirumamilla M, Miele E, Coluccio ML, La Rocca R, Brescia R, Krahn R, Das G, De Angelis F, Liberale C, Toma A, Razzari L, Manna L, Proietti Zaccaria R. In: Hashim AA, editor. *The Delivery of Nanoparticles*. Rijeka: Intech; 2012. p. 293. DOI: 10.5772/2647
- [38] Ou FS, Hu M, Naumov I, Kim A, Wu W, Bratkovsky AM, Li X, Williams RS, Li Z. Hot-spot engineering in polygonal nanofinger assemblies for surface enhanced Raman spectroscopy. *Nano Letters*. 2011;**11**:2538. DOI: 10.1021/nl201212n

- [39] Jung K, Hahn J, In S, Bae Y, Lee H, Pikhitsa PV, Ahn K, Ha K, Lee J-K, Park N, Choi M. Hotspot-engineered 3D multipetal flower assemblies for surface-enhanced Raman spectroscopy. *Advanced Materials*. 2014;**26**:5924. DOI: 10.1002/adma.201401004
- [40] Forestiere C, Pasquale AJ, Capretti A, Miano G, Tamburrino A, Lee SY, Reinhard BM, Dal Negro L. Genetically engineered Plasmonic Nanoarrays. *Nano Letters*. 2012;**12**:2037. DOI: 10.1021/nl300140g
- [41] Kleinman SL, Frontiera RR, Henry A-I, Dieringer JA, Van Duyne RP. Creating, characterizing, and controlling chemistry with SERS hot spots. *Physical Chemistry Chemical Physics*. 2013;**15**:21. DOI: 10.1039/C2CP42598J
- [42] Fabris L. Bottom-up optimization of SERS hot-spots. *Chemical Communications*. 2012;**48**:9346. DOI: 10.1039/C2CC34068B
- [43] Chirumamilla M, Gopalakrishnan A, Toma A, Proietti Zaccaria R, Krahn R. Plasmon resonance tuning in metal nanostars for surface enhanced Raman scattering. *Nanotechnology*. 2014;**25**:235303. DOI: 10.1088/0957-4484/25/23/235303
- [44] Yuan H, Wilson CM, Xia J, Doyle SL, Li S, Fales AM, Liu Y, Ozaki E, Mulfaul K, Hanna G, Palmer GM, Wang LV, Grant GA, Vo-Dinh T. Plasmonics-enhanced and optically modulated delivery of gold nanostars into brain tumor. *Nanoscale*. 2014;**6**:4078. DOI: 10.1039/C3NR06770J
- [45] Fredriksson H, Alaverdyan Y, Dmitriev A, Langhammer C, Sutherland DS, Zäch M, Kasemo B. Hole-mask colloidal lithography. *Advanced Materials*. 2007;**19**:4297. DOI: 10.1002/adma.200700680
- [46] Proietti Zaccaria R, Toma A, Das G, Giugni A, Tuccio S, Panaro S, Chirumamilla M, Gopalakrishnan A, Saeed A, Li H, Krahn R, Di Fabrizio E. In: Boriskina SV, Zheludev NI, editors. *Singular and Chiral Nanoplasmonics*. USA: Pan Stanford; 2014. p. 451. DOI: 10.4032/9789814613187
- [47] Huck C, Toma A, Neubrech F, Chirumamilla M, Vogt J, De Angelis F, Pucci A. Gold nanoantennas on a pedestal for plasmonic enhancement in the infrared. *ACS Photonics*. 2015;**2**:497. DOI: 10.1021/ph500374r

